Nanoscale Horizons

ROYAL SOCIETY OF CHEMISTRY

COMMUNICATION

View Article Online
View Journal | View Issue

Cite this: *Nanoscale Horiz.*, 2025, 10, 3469

Received 21st July 2025,
Accepted 12th September 2025

DOI: 10.1039/d5nh00515a

rsc.li/nanoscale-horizons

Second-harmonic generation and photoluminescence properties of colloidal WS_2 monolayers deposited from solution

Yang Zhao,†[ab] Markus Fröhlich,†[a] Marco Kögel,[c] Onno Strolka,[ade] André Niebur,[de] Tim Parker,[ab] Felix Schneider,[ab] Alfred J. Meixner,[ab] Jannik C. Meyer,[cf] Dai Zhang *[ab] and Jannika Lauth *[abde]

Monolayered WS_2 exhibits a direct band gap, strongly bound excitons, trions and biexcitons as well as no inversion symmetry in the 2D crystal structure (D_{3h}), allowing frequency doubling by second-harmonic generation. The recent progress in colloidal synthesis of transition metal dichalcogenides enables the scalable production of phase-pure monolayer-dominated WS_2. In this work, we use parabolic mirror-assisted microscopy to investigate the linear and nonlinear optical properties of deposited colloidal WS_2. Spatial and spectral resolution of one- and two-photon photoluminescence and second-harmonic generation correlates structural motifs of the WS_2 layers including orientation and agglomeration to the local optical response. We find exciton and trion emission at 613 nm and 639 nm respectively, with significantly varying contribution to the overall intensity between one- and two-photon excitation. This is attributed to the increased carrier density under high fluences needed for two-photon excitation. By evaluating the second-harmonic generation intensity, the nonlinear susceptibility of colloidally synthesized WS_2 nanosheets is calculated to range from 4.28–7.55 nm V^{-1}, averaging higher than a commercial WS_2 monolayer reference sample. Our results show that colloidal WS_2 is suitable for large area coverage creating an isotropic WS_2 film, while retaining the highly sought after linear and nonlinear optical properties of WS_2 monolayers, even under surface ligand separated aggregation.

New concepts

Research on transition metal dichalcogenides (TMDCs) is dominated by individual monolayers (MLs) of typically exfoliated and/or CVD-grown WS_2 flakes. Building on our recent advances in the wet-chemical synthesis of TMDCs, organic-ligand separated WS_2 nanosheet (NS) MLs are synthesized. We then use parabolic mirror-assisted microscopy to characterize the photoluminescence (PL), two-photon photoluminescence and second-harmonic generation (SHG) of deposited colloidal WS_2 NSs with spatial resolution, allowing us to correlate the local structure with spectral and temporal information of colloidal TMDCs for the first time. Depending on the polarized excitation, the orientation of individual WS_2 NSs within the ensemble is revealed. By phasor plot analysis of PL lifetimes, we disentangle emission stemming from WS_2 NSs and residual ligands. WS_2 NSs are characterized by HR-TEM, Raman-, absorption and PL spectroscopy, underpinning that they retain ML properties in solution and when deposited. Highly efficient second-harmonic generation (SHG, 4.28–7.55 nm V^{-1}) from colloidally synthesized WS_2 NSs exceeds benchmark CVD samples and shows that they are solution-processable and scalable, enabling their future integration into fiber optics or biological systems as contrast agents for enhanced resolution SHG-microscopy. Characterizing the properties, applicability and limitations of wet-chemically synthesized WS_2 NSs is the first step for colloidal TMDCs as innovative nonlinear materials.

Introduction

WS_2 has been studied for its wide range of possible applications from catalysis over sensing to a variety of different electronic and optoelectronic applications including transistors and lasers.[2–5] WS_2 shows strong excitonic absorption and emission at room temperature with high binding energies (up to 0.7 eV) and an indirect (bulk) to direct band gap (2.02 eV) transition, when monolayer (ML) thickness is reached.[6–9] The optical features of WS_2 MLs in the ultraviolet and visible (UV-Vis) spectral range exhibit four excitonic transitions. The direct transitions A and B located at 614 and 517 nm emerge from

[a] *Institute of Physical and Theoretical Chemistry, Eberhard Karls University of Tübingen, Auf der Morgenstelle 18, D-72076 Tübingen, Germany. E-mail: jannika.lauth@uni-tuebingen.de*
[b] *Center for Light-Matter-Interaction, Sensors, and Analytics (LISA+), Eberhard Karls University of Tübingen, Auf der Morgenstelle 15, D-72076 Tübingen, Germany*
[c] *Natural and Medical Sciences Institute (NMI) at the Eberhard Karls University of Tübingen, Markwiesenstraße 55, D-72770 Reutlingen, Germany*
[d] *Institute of Physical Chemistry and Electrochemistry, Leibniz University Hannover, Callinstr. 3A, D-30167 Hannover, Germany*
[e] *Cluster of Excellence PhoenixD (Photonics, Optics, and Engineering – Innovation Across Disciplines), Welfengarten 1A, D-30167 Hannover, Germany*
[f] *Institute of Applied Physics, Eberhard Karls University of Tübingen, Auf der Morgenstelle 10, D-72076 Tübingen, Germany*
† Yang Zhao and Markus Fröhlich contributed equally.

split valence bands at the K point in the Brillouin zone, while at higher energies the indirect C and D transitions can be observed at 436 and 364 nm, resp.[10–12] Photoluminescence (PL) spectra of WS_2 MLs are complex with several contributions from A and B excitons, trions and/or biexcitons.[13–16] While previous studies found the neutral A excitons to recombine mainly radiatively and give rise to one-photon PL, non-radiative recombination is commonly observed from excitonic complexes.[17] Sulfur vacancies are ubiquitous defects in WS_2 resulting in negative doping and therefore facilitate the formation of negative trions as well as Auger recombination, which suppresses PL and thereby limits the application of colloidal WS_2 nanosheets (NSs).[18–20] Nonlinear optical properties of WS_2 such as two-photon photoluminescence (2PPL) have also been explored.[21–23] Applying 2PPL, Ye *et al.* revealed excitonic dark states in WS_2 MLs, which cannot be probed by one photon PL.[24] Second-harmonic generation (SHG) is a higher-order light–matter interaction process where an incoming fundamental electromagnetic wave with a frequency ω is converted *via* a virtual state to light of double the frequency 2ω (see Fig. S1 in the SI). The SHG intensity depends on how well the phase matching condition is met, thus requiring a material without inversion symmetry.[10,25–27] When reduced from bulk (D_{6h} symmetry) to ML thickness (D_{3h} symmetry), WS_2 shows a remarkably high SHG, varying greatly between odd and even layered samples.[10,28] Laterally translated or defected crystal structures as well as strain and twist angles break the symmetry of even-layers in 2H-phase TMDCs, hence also allowing SHG to emerge from an originally non-SHG active system.[29,30]

So far, 2D TMDC mono- and few layers are typically obtained by top-down processes, previously established for graphene by exfoliating the monolayers using the scotch tape method or liquid phase exfoliation.[31–33] Bottom-up methods include chemical vapor deposition (CVD) and wet-chemical synthesis of WS_2 MLs.[34] The latter enables a scalable production of solution processed colloidal NSs, while maintaining high control over the crystal phase, size and layer number as well as the tunability of optical properties and the elemental composition.[35–40] Recently, the linear optical properties of colloidal TMDCs (2D WS_2 and MoS_2 NSs) and laterally smaller nanoplatelets have been characterized at room- and cryogenic temperatures, underpinning the ability to wet-chemically synthesize photoluminescent TMDC NSs.[38,41,42] However, the nonlinear optical properties of colloidal WS_2 NSs lack investigation up to now.

Here, we describe the 2PPL and SHG properties of wet chemically synthesized WS_2 NSs in detail and evaluate the relationship between local structure motifs and the optical response under radial-, azimuthal- and linear-excitation polarization. We determine the nonlinear susceptibility (NLS) of colloidal WS_2 NSs based on their power-dependent SHG intensity and compare it to a CVD grown WS_2 flake. By applying phasor plot analysis to fluorescence lifetime data, PL contributions of excess ligands are separated from the PL of WS_2. We find that colloidal WS_2 NSs exhibit optical properties comparable to CVD grown flakes, with added scalability and flexible application to different substrates/host-matrices. Our results paint a promising picture for future implementation of colloidal WS_2 NSs in nonlinear optoelectronics such as optical modulators, optical switching and high-density storage devices.[43–46]

Results and discussion

The colloidal WS_2 NSs characterized here are synthesized wet-chemically by the dropwise addition of the tungsten-precursor consisting of WCl_6 dissolved in oleylamine (OlAm) to a pre-heated solution of elemental sulfur/OlAm under inert conditions as has been described in our previous work (detailed information on the synthesis and sample preparation as well as the chemicals used can be found in the SI, Section A and B).[39,42]

To confirm the synthesis of predominantly monolayered 2H-phase WS_2 NSs, we use a combination of (high-resolution) transmission electron microscopy (HR-TEM), scanning electron microscopy (SEM) and optical spectroscopy (UV-vis absorption, PL and Raman), covering the microscopic to the ensemble level range. HR-TEM in Fig. 1a shows an example of a flat lying ML as well as different twisted bilayers (Moiré pattern). The fast Fourier transform (FFT) insets in the left and right corners show the hexagonal pattern of the semiconducting WS_2 2H-phase around the (001) crystal plane axis. Due to agglomeration during the drying process on the substrate, so-called nanoflowers are formed on the μm scale as is shown by SEM in the inset in Fig. 1a. These porous structures consist of a multitude of individual NSs each sized 18.4 ± 6 nm as is evident from the HR-TEM images in Fig. 1a and Fig. S3b (the size distribution is given in Fig. S2). The solvent (OlAm) can also act as a L-type ligand and helps to keep individual WS_2 NSs from stacking into bulk material in solution and in the deposited film. Examples of ligand-separated WS_2 NSs are shown in Fig. S3a. Here, the inter layer distance within the nanoflower varies. In contrast to the bulk distance of WS_2 bilayers of 0.3 nm,[47] typically closely aligned NSs are 1–3 nm apart, underpinning efficient ligand separation.

Fig. 1b displays the absorbance spectrum of colloidal WS_2 NSs in solution (see Fig. S4 for deposited sample). The A, B, C and D excitonic transitions (614 nm (2.02 eV); 517 nm (2.40 eV); 436 nm (2.84 eV) and 364 nm (3.41 eV)) are observed. The second derivative of the absorbance spectrum is plotted for better visibility and spectral separation of C and D excitonic absorption. Raman spectroscopic measurements confirm the ML thickness of the colloidal WS_2 NSs to be retained in the dried state as well as the associated 2H-phase purity shown in Fig. 1c. The spectrum is dominated by first-order modes including the longitudinal acoustic mode LA(M) at 179.4 cm^{-1} at the M point in the Brillouin zone, which is related to the in-plane collective movements of the atoms in the lattice, while the A_{1g} feature at 415.4 cm^{-1} corresponds to the out-of-plane phonon mode for two adjacent layers.[1,48] The strongest peak at 352.3 cm^{-1} consists of two subpeaks, which are identified by multipeak Gaussian fitting to correspond to the in-plane vibrational E^1_{2g}(M) mode, and the second-order longitudinal acoustic phonon 2LA(M) mode. The subpeaks between ~290 and 330 cm^{-1} consist of

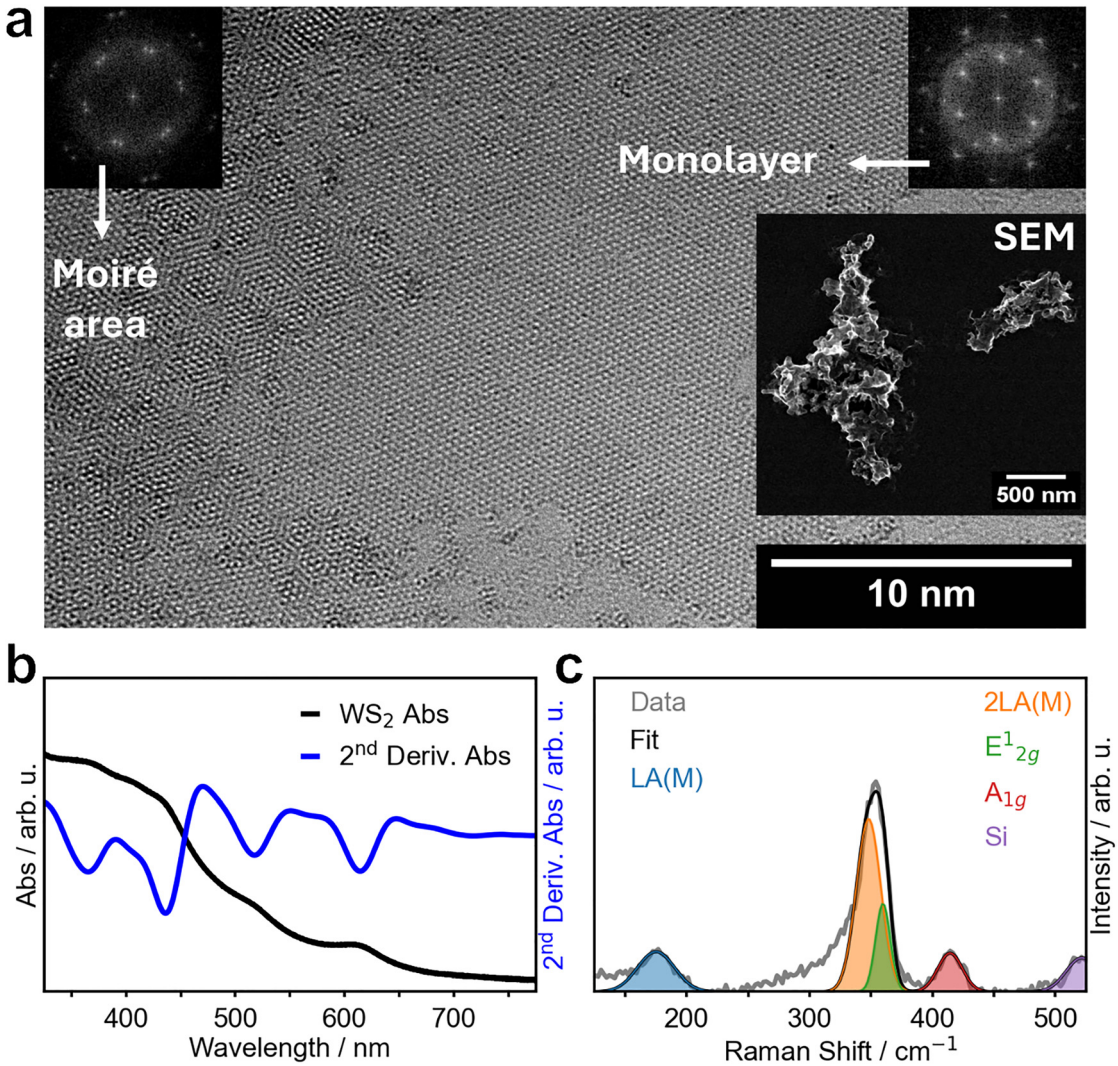

Fig. 1 (a) HR-TEM of drop-casted colloidal WS_2 NSs with SEM inset showing agglomerated NSs on the substrate in lower magnification. The FFT insets show a hexagonal WS_2 structure for the ML area as well as the Moiré area. (b) Absorption of colloidal WS_2 NSs in 1,2-dichlorobenzene showing A, B, C and D excitonic shoulders (black) and second derivative of the absorption plotted for better visibility of the C and D excitonic features (blue). (c) Fitted Raman spectrum of drop-casted WS_2 NSs measured under linear laser polarization with E^1_{2g} and A_{1g} modes found at WS_2 ML wavenumbers.[1]

several unassigned peaks beneath the spectral resolution limit of our setup (and are not vital for the following discussion). The frequencies of the E^1_{2g} and A_{1g} modes match WS_2 ML values,[1] while the intensity at $\sim$352.0 cm^{-1} is roughly twice that of the A_{1g} mode. The high intensity at $\sim$352.0 cm^{-1} is due to the 2LA(M) acoustic mode, which only arises in ML WS_2 and is matching the frequency of the E^1_{2g}, thereby adding onto the peak at $\sim$352.0 cm^{-1}.[48] This shows a substantial ML content in the colloidal WS_2 NS ensemble and compliments the microscopic evaluation from individual NSs by TEM. The removal of excess OlAm ligand (as is described in the SI, Section B), is assessed by phasor plot analysis of the lifetime distribution from the as-synthesized and subsequently washed WS_2 NSs (see Fig. S5 for a schematic description). The presences of excess OlAm, shown as green areas in Fig. S6a, are clearly identified in the fluorescence lifetime phasor plot analysis as a long lifetime component. The successful removal of excess OlAm ligand from the WS_2 NSs after repeated rinsing with hexane and isopropanol is confirmed in Fig. S6b by the general absence of long lifetime components. The shorter lifetime of WS_2 NSs is highlighted red.

To investigate the relationship between the one-photon PL and local morphology of WS_2 nanoflowers, polarized excitation experiments were performed using the home-built parabolic mirror-assisted optical setup shown in Fig. S7. Additionally to the commonly used linear polarization, radially polarized donut mode (RPDM) and azimuthally polarized donut mode (APDM) were also applied, as they are well-suited for studying materials with preferred dipole orientations due to their distinct electric field distributions in the focal plane (Fig. S8).[49,50] In the focus of a linearly polarized beam (Fig. S8a) both transverse components and longitudinal components are present. RPDM on the other hand, exhibits a dominant longitudinal component E_z perpendicular to the focal plane (Fig. S8b), hence it can be used to efficiently excite the out-of-plane dipole moment. In contrast,

APDM produces only a transverse field parallel to the focal plane $E_{x,y}$ (Fig. S8c), which is ideal for exciting in-plane oriented dipole moments. The dark-field scattering image in Fig. 2a shows the unordered agglomeration of many single drop-casted WS_2 NSs into nanoflowers. We correlate this dark-field optical image with the PL maps shown in Fig. 2c and d in which the PL intensity distribution is inhomogeneous under excitation with RPDM and APDM. Though the electric field distribution in the focus of RPDM and APDM is distinctively different, the PL intensity of WS_2 NS nanoflowers is rather comparable. We hence infer an isotropic arrangement of WS_2 NSs in the agglomerated structure. However, some regions indeed show excitation-dependent PL (marked by the white arrows in Fig. 2d). These areas excited by the APDM show higher PL intensity than the corresponding regions excited by RPDM in Fig. 2c, which indicates the presence of many or exceptionally bright flat-lying WS_2 NSs traced by the $E_{x,y}$ electric component present in the focus in APDM.

In our previous work, we described the first μ-PL of wet chemically synthesized WS_2 MLs.[42] Here, we use spatially, temporally and spectroscopically resolved methods to further disentangle the single PL contributions. By exciting the A and B excitonic transitions with a 532 nm continuous wave laser, μ-PL is detected at 613 nm (2.02 eV, see Fig. 2b). This observation is consistent with experimentally observed and calculated optical band gaps for WS_2 MLs.[6,24,51] To assign the origin of the PL signal, we extract the excitonic subpeaks by Gaussian fits.[52,53] The result in Fig. 2b contains three fitted subpeaks at 613 nm (2.02 eV), 639 nm (1.94 eV) and 670 nm (1.85 eV), resp. Previous studies by Cui *et al.* and Kato *et al.* on WS_2 allow for the assignment of the peaks to a neutral exciton (X_A), a negatively charged trion (X_A^-) and defect related excitons (X_D) originating from sulfur vacancies and exposed vacant sites on the edges of the WS_2 NSs.[54–58] To enhance the statistical validity, we compare excitonic peaks in other sample regions (see Fig. S9). In all cases, the emission of X_A dominates the PL spectra with the trion PL as the second most intense contribution. The overall intensity may vary from spot to spot (as is evident from the maps in Fig. 2c and d) due to the heterogeny of the nanoflower structure, but the spectral features of the individual NSs stay consistent.

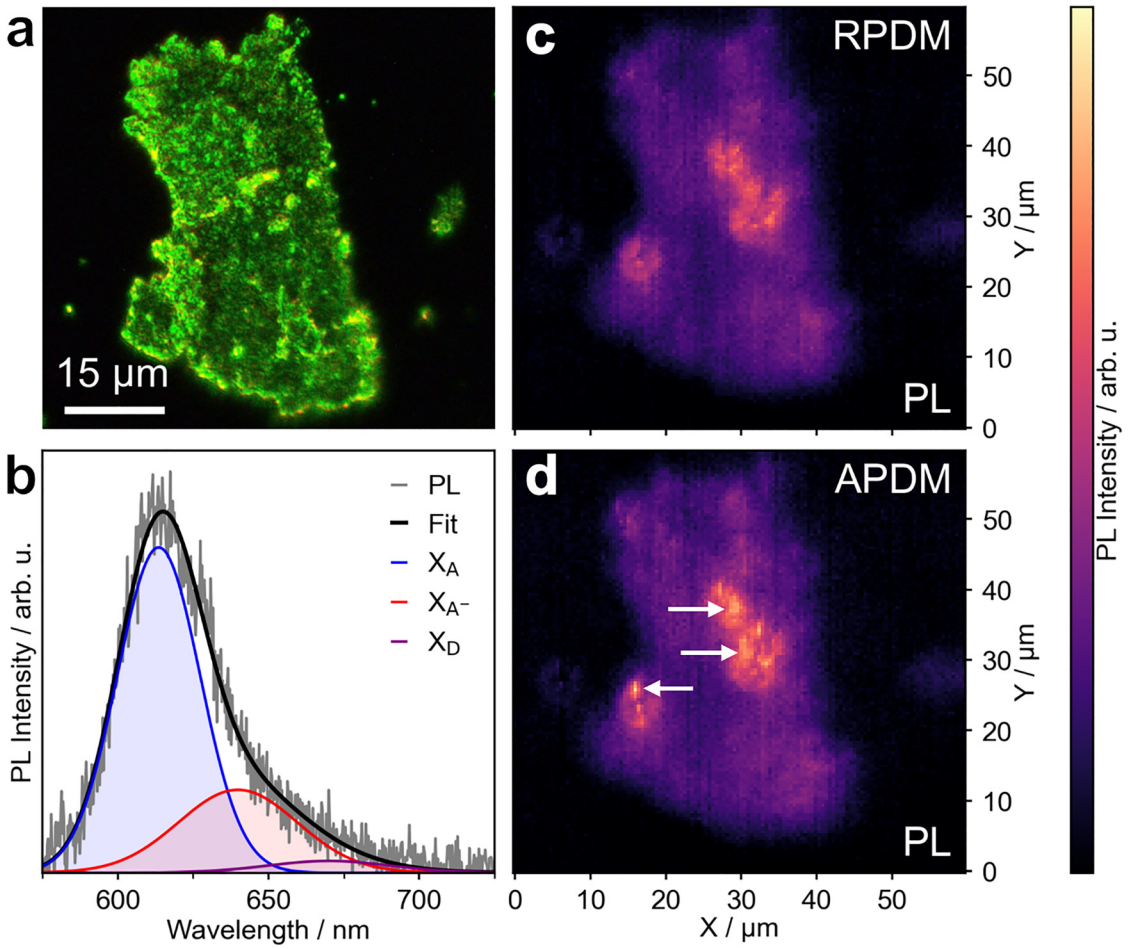

Fig. 2 (a) Dark-field optical image of a WS_2 NSs agglomerate. (b) PL spectrum of WS_2 nanoflowers collected under APDM with fitted subpeaks, which can be attributed to X_A, X_A^-, and X_D. (c) and (d) PL intensity maps of WS_2 NS agglomerate shown in (a) under RPDM and APDM excitation, resp. White arrows highlight spots that are particularly bright under APDM excitation and indicate possibly flat-lying NSs with increased polarization-dependent PL intensity in APDM.

Further, we excited the same WS_2 NS agglomerate with high intensity femtosecond laser pulses to study its nonlinear optical response including 2PPL and SHG. Fig. 3a shows the 2PPL signal of a WS_2 NS agglomerate. The origin of the PL here is exclusively nonlinear because the excitation energy (779 nm, 1.59 eV) is lower than the bandgap of ML WS_2 (2.02 eV). Compared to linearly polarized and RPDM excitation, the 2PPL image excited by APDM shows a particularly high intensity and a distinctly inhomogeneous intensity distribution, indicating the presence of many or exceptionally bright flat-lying WS_2 NSs selectively excited by the APDM. Fig. 3b shows the SHG of WS_2 NSs under three different excitation polarizations. While the distribution of the SHG intensity under linear polarization (LP) or RPDM excitation is quite homogeneous, the SHG under APDM appears slightly more intense in the regions where the 2PPL is high (see Fig. 3a for comparison). Since SHG is strongly dependent on the local crystal structure and orientation of the WS_2 NSs, we assume an increased SHG signal results from flat-lying WS_2 NSs by APDM excitation. Fig. 3c clearly shows a sharp SHG peak at 389.5 nm, which is the frequency-doubled fundamental excitation laser wavelength (779 nm), as well as the 2PPL signal together with a broad background

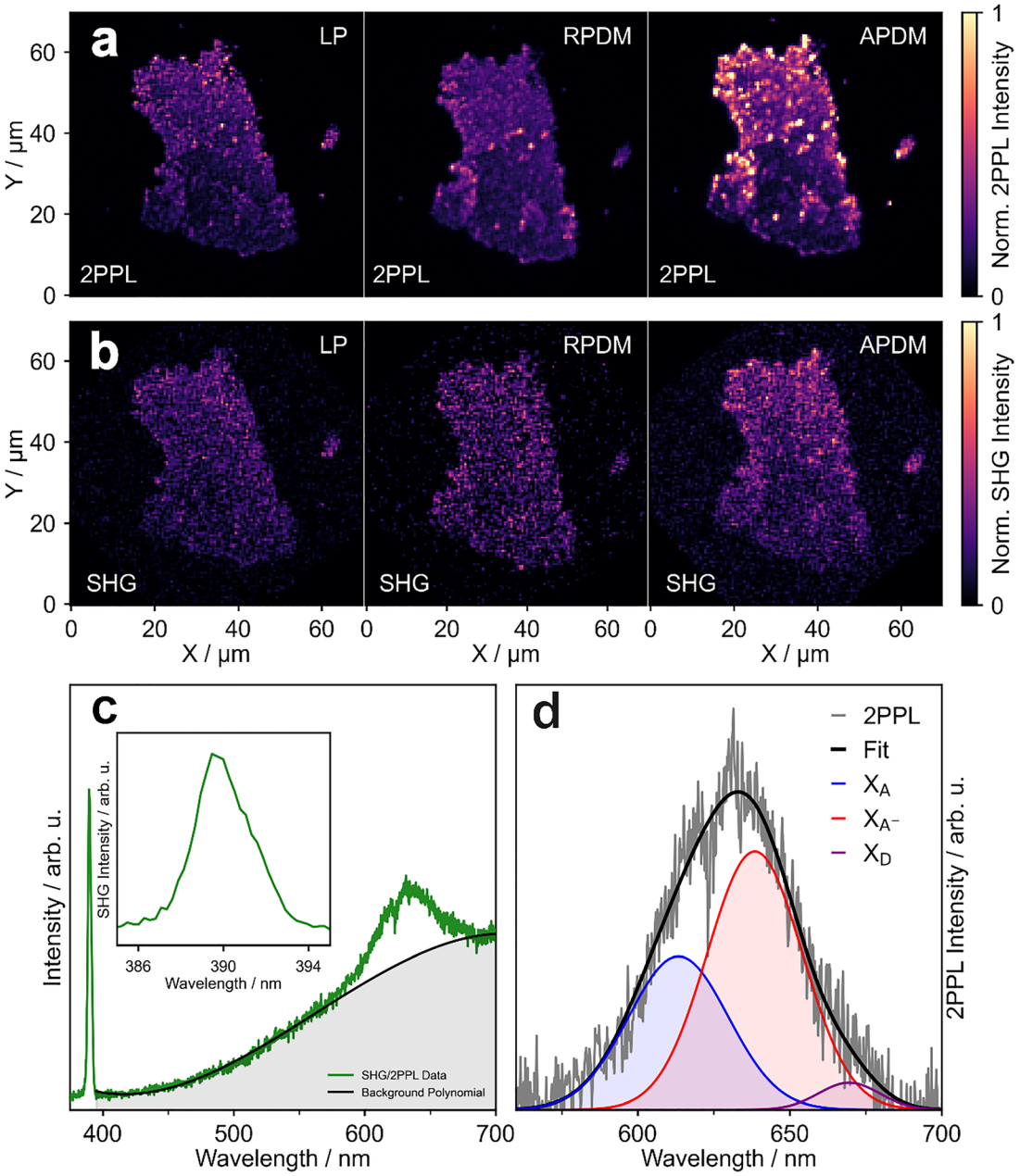

Fig. 3 (a) 2PPL intensity maps of WS_2 NS an agglomerate under LP, RPDM and APDM, resp. (b) SHG intensity maps of WS_2 NSs an agglomerate under LP, RPDM and APDM, resp. (c) 2PPL and SHG spectrum as collected by the nonlinear setup under APDM excitation. A background polynomial is fitted to allow subsequent fitting of the 2PPL contributions. (d) Fitted 2PPL spectrum (extracted from 3c) with three peaks associated to X, X_{A^-}, and X_D.

feature. We fitted the background with a third order polynomial to be able to extract the excitonic contributions of the 2PPL in Fig. 3d. In comparison to the PL spectrum (Fig. 2b), three subpeaks corresponding to 613 nm (X_A), 639 nm (X_{A^-}) and 670 nm (X_D) are fitted to the 2PPL. Interestingly, unlike in the one-photon PL (Fig. 2b), where the neutral excitonic feature dominates, the 2PPL spectra are dominated by trion emission for most sample regions (seen in S10). Comparing these findings with literature, a similar result is found also for exfoliated WS_2 MLs.[59] A reason for this could be the high peak power of the femtosecond pulsed laser used for the two-photon absorption experiments, which may result in a higher charge carrier density, thereby increasing the likelihood of trion formation.[60,61]

Finally, to quantify the nonlinear susceptibility (NLS), we followed the theoretical surface SHG formalism of Shen *et al.* and converted equations from Woodward *et al.*'s work.[62,63] Previously we have used the same method to calculate the NLS of Nb_3SeI_7 flakes.[64] The precondition that the light is at normal incidence to the sample and the contribution by the nonlinearity of air or substrate (mainly the effect from dispersion) is neglected are applied.

The specific equations used in the NLS calculation are:

$$I_{\mathrm{SHG}}(2\omega) = \frac{1}{\varepsilon_0}\left[\frac{1}{2c}\left(\frac{2}{1+n_2}\right)^2\right](2\omega)^2\left|\chi_s^{(2)}\right|^2 I_1^2(\omega) \quad (1)$$

$$P_{\mathrm{SHG\,max}}(2\omega) = \frac{16\sqrt{2}S\left|\chi_s^{(2)}\right|^2\omega^2}{c^3\varepsilon_0 f\pi r^2 t_{\mathrm{FWHM}}(1+n_2)^6}P_1^2(\omega) \quad (2)$$

where ε_0 is the permittivity of vacuum, c is the speed of light in vacuum, n_2 is the refractive index (1.45–1.50), ω is the pump angular frequency, $I_1(\omega)$ is the focused pump peak intensity in air, $|\chi_s^{(2)}|$ is the magnitude of the sheets' susceptibility for second-order nonlinearity, f is the pump laser repetition rate, S is a shape factor for the Gaussian pulse applied in the setup, t_{FWHM} is the pulse full width at half maximum, and $P_1(\omega)$ is the average pump power.

Since the parameters related to the setup configuration are fixed during all susceptibility measurements, the equations can be reduced to eqn (3) (detailed derivation process and specific parameters are shown in eqn (S9), (S10) and (S11) in the SI):

$$\left|\chi_{s\text{-}WS_2\ NSs}^{(2)}\right| = \sqrt{\frac{\frac{I_{\mathrm{SHG\,max}}(2\omega_{WS_2\ NSs})}{P_1^2(\omega_{WS_2\ NSs})}}{\frac{I_{\mathrm{SHG\,max}}(2\omega_{WS_2\text{-Ref. Flake}})}{P_1^2(\omega_{WS_2\text{-Ref. Flake}})}}}\left|\chi_{s\text{-}WS_2\text{-Ref. Flake}}^{(2)}\right| \quad (3)$$

The ratio of NLS is calculated by the power-dependent SHG intensity measurements on the WS_2 NSs and CVD grown WS_2 flakes (optical characterization of the CVD grown WS_2 flakes can be found in Fig. S11). According to work by Janisch *et al.*,[65] CVD grown WS_2 on a SiO_2/Si substrate exhibit intense NLS, as high as 4.50 nm V^{-1} at 832 nm, which we use as reference value.

For the power-dependent SHG measurements, we employed excitation powers ranging from 0.8 to 8 mW corresponding to 52.1 to 521 GW cm^{-2} of in-focus peak-power, considering a Gaussian beam distribution of the femtosecond pulsed laser system under the Rayleigh diffraction limit condition (calculated in the SI, Section B). Fig. 4a shows that the SHG intensity of all WS_2 samples studied is proportional to the squared excitation power, agreeing well with eqn (2). For each power, five spots are measured and averaged. Their deviation is indicated by the error bars. The magnitude of the slopes ranges from 116 to 141 for our WS_2 NSs and from 84 to 120 for the CVD sample, showing the significantly higher nonlinear response of the colloidally synthesized WS_2 NS sample (Fig. 4b). We observed the NSs to be subject to damage (as indicated by the muted color datapoints in Fig. 4a) at high power above 40 mW^2. Since the CVD-grown reference sample did not show signs of damage, we suspect the damage to originate from burning (carbon build-up) or evaporation of the OlAm ligands that stabilize the NSs due to local heating by the high intensity laser. Note that the observed damage threshold at >36 mW^2 (391 GW cm^{-2}) is beyond usual operating power, as is evident from similar reports,[66,67] which mitigates applicability risks. Following eqn (3), we can derive the relative NLS of the deposited colloidal WS_2 NSs. Comparing the slope values and taking the reference NLS value of CVD-grown WS_2 MLs (4.50 nm V^{-1}) into account,[65] the NLS lies in the range of 4.28 to 7.55 nm V^{-1}.

Conclusions

We have characterized the linear and nonlinear optical properties of colloidal WS_2 NSs samples, which are ML-dominated as is shown by HR-TEM, absorption, Raman and PL spectroscopy. Polarization-dependent PL measurements indicate that the emission of WS_2 NSs is dominated by neutral excitons (X_A) with an intensity distribution which is non-uniform but comparable under RPDM and APDM excitation, which suggests the

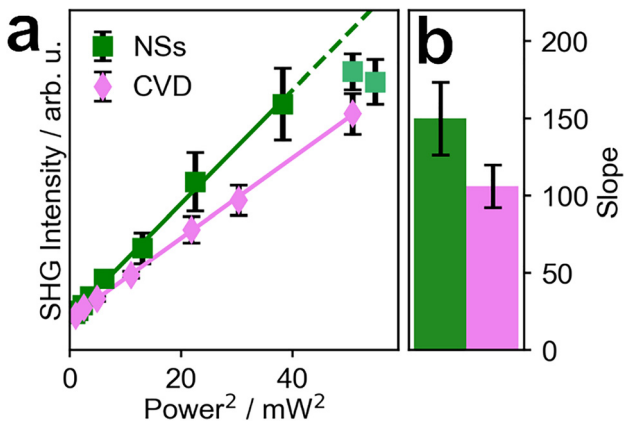

Fig. 4 (a) Power-dependent SHG intensity collected on deposited WS_2 NSs. At high intensity, the WS_2 NSs exhibit signs of photodamage (b) calculated slopes of WS_2 NSs and CVD grown WS_2 flakes shown in (a) with deposited WS_2 NSs exhibiting a higher response on average.

WS_2 NSs to be isotropically oriented. The same concept applies to the intense SHG of WS_2 NSs, which is only weakly influenced by polarized excitation. However, differences in the local crystal structure and dipole orientation still cause minor polarization-related changes. The 2PPL signal of colloidal WS_2 NSs, in contrast to the one-photon PL exhibits an increased amount of trion emission (X_{A^-}), which could be caused by the high intensity femtosecond pulsed laser excitation. Other contributions stemming from excess OlAm ligand adsorbed to the nanoflower surface were identified and removed using phasor plot analysis of the PL lifetime data.

Drop-casted colloidal WS_2 MLs exhibit high NLS (4.28 to 7.55 nm V^{-1}), thereby achieving an equal or higher NLS response than comparable CVD grown single WS_2 MLs and rendering them a scalable solution-processed SHG material alternative.

Author contributions

Synthesis, characterization (UV-Vis Abs-, Raman-, SEM-, TEM-evaluation) and sample preparation was done by M. F. with initial experiments by O. S. and both supervised by J. L. Low res. TEM images were obtained by A. N. under supervision by J. L. High res. TEM images were obtained by M. K. under supervision by J. C. M. Y. Z. performed the PL, 2PPL, FLIM, SHG and Raman experiments and the related data analysis. T. P. and F. S. assisted the linear and nonlinear optical measurements. D. Z. supervised the PL, 2PPL FLIM, and SHG experiments and the data analysis. Y. Z., M. F., D. Z. and J. L. conceptualized the manuscript. All authors commented on the draft. A. J. M., J. M., D. Z. and J. L. obtained the funding.

Conflicts of interest

There are no conflicts to declare.

Data availability

The data supporting this article has been included as part of the supplementary information (SI). Supplementary information: additional figures and data. See DOI: **https://doi.org/10.1039/d5nh00515a**.

All other relevant data are available from the corresponding authors upon reasonable request.

Acknowledgements

Y. Z. thanks the Chinese Scholarship Council for financial support. D. Z. acknowledges funding by the German Research Foundation (ZH279/13-1). J. L. gratefully acknowledges funding by the German Research Foundation under the Excellence Strategy of the Cluster of Excellence PhoenixD (EXC 2122, Project ID 390833453). J. L. is also grateful for additional funding by an Athene Grant of the University of Tübingen (by the Federal Ministry of Education and Research (BMBF) and the Baden-Württemberg Ministry of Science as part of the Excellence Strategy of the German Federal and State Governments).

Notes and references

1 S. Qiao, H. Yang, Z. Bai, G. Peng and X. Zhang, *Adv. Eng. Res.*, 2017, **141**, 1408–1413.
2 K. P. J. Thomas, F. Jaramillo, J. Bonde, J. H. Nielsen, S. Horch and I. Chorkendorff, *Science*, 2007, **317**, 100–102.
3 R. Kumar, W. Zheng, X. Liu, J. Zhang and M. Kumar, *Adv. Mater. Technol.*, 2020, **5**, 1901062.
4 B. Radisavljevic, A. Radenovic, J. Brivio, V. Giacometti and A. Kis, *Nat. Nanotechnol.*, 2011, **6**, 147–150.
5 Y. Ye, Z. J. Wong, X. Lu, X. Ni, H. Zhu, X. Chen, Y. Wang and X. Zhang, *Nat. Photonics*, 2015, **9**, 733–737.
6 B. Zhu, X. Chen and X. Cui, *Sci. Rep.*, 2015, **5**, 9218.
7 K. F. Mak, C. Lee, J. Hone, J. Shan and T. F. Heinz, *Phys. Rev. Lett.*, 2010, **105**, 136805.
8 Y. Ma, Y. Dai, M. Guo, C. Niu, J. Lu and B. Huang, *Phys. Chem. Chem. Phys.*, 2011, **13**, 15546–15553.
9 A. Splendiani, L. Sun, Y. Zhang, T. Li, J. Kim, C. Y. Chim, G. Galli and F. Wang, *Nano Lett.*, 2010, **10**, 1271–1275.
10 H. Zeng, G. B. Liu, J. Dai, Y. Yan, B. Zhu, R. He, L. Xie, S. Xu, X. Chen, W. Yao and X. Cui, *Sci. Rep.*, 2013, **3**, 1608.
11 A. Carvalho, R. M. Ribeiro and A. H. Castro Neto, *Phys. Rev. B: Condens. Matter Mater. Phys.*, 2013, **88**, 115205.
12 T. Goswami, H. Bhatt, K. J. Babu, G. Kaur, N. Ghorai and H. N. Ghosh, *J. Phys. Chem. Lett.*, 2021, **12**, 6526–6534.
13 G. Plechinger, P. Nagler, J. Kraus, N. Paradiso, C. Strunk, C. Schüller and T. Korn, *Phys. Status Solidi RRL*, 2015, **9**, 457–461.
14 S. Golovynskyi, O. I. Datsenko, D. Dong, Y. Lin, I. Irfan, B. Li, D. Lin and J. Qu, *J. Phys. Chem. C*, 2021, **125**, 17806–17819.
15 A. Boulesbaa, B. Huang, K. Wang, M.-W. Lin, M. Mahjouri-Samani, C. Rouleau, K. Xiao, M. Yoon, B. Sumpter, A. Puretzky and D. Geohegan, *Phys. Rev. B: Condens. Matter Mater. Phys.*, 2015, **92**, 115443.
16 P. Miao, Y. T. Chen, L. Pan, A. Horneber, K. Greulich, T. Chasse, H. Peisert, P. M. Adam, P. Xu, A. Meixner and D. Zhang, *J. Chem. Phys.*, 2022, **156**, 034702.
17 D.-H. Lien, S. Z. Uddin, M. Yeh, M. Amani, H. Kim, J. W. Ager III, E. Yablonovitch and A. Javey, *Science*, 2019, **364**, 468–471.
18 H. Qiu, T. Xu, Z. Wang, W. Ren, H. Nan, Z. Ni, Q. Chen, S. Yuan, F. Miao, F. Song, G. Long, Y. Shi, L. Sun, J. Wang and X. Wang, *Nat. Commun.*, 2013, **4**, 2642.
19 L. Li, M. F. Lin, X. Zhang, A. Britz, A. Krishnamoorthy, R. Ma, R. K. Kalia, A. Nakano, P. Vashishta, P. Ajayan, M. C. Hoffmann, D. M. Fritz, U. Bergmann and O. V. Prezhdo, *Nano Lett.*, 2019, **19**, 6078–6086.
20 M. R. Rosenberger, H. J. Chuang, K. M. McCreary, C. H. Li and B. T. Jonker, *ACS Nano*, 2018, **12**, 1793–1800.
21 Y.-Z. Lan and X.-H. Bao, *Phys. Rev. B: Condens. Matter Mater. Phys.*, 2020, **101**, 195437.

22 S. Karmakar, U. Chatterjee and P. Kumbhakar, *Opt. Laser Technol.*, 2021, **136**, 106696.
23 H. Long, L. Tao, C. Y. Tang, B. Zhou, Y. Zhao, L. Zeng, S. F. Yu, S. P. Lau, Y. Chai and Y. H. Tsang, *Nanoscale*, 2015, **7**, 17771–17777.
24 Z. Ye, T. Cao, K. O'Brien, H. Zhu, X. Yin, Y. Wang, S. G. Louie and X. Zhang, *Nature*, 2014, **513**, 214–218.
25 W. J. Schutte, J. L. D. Boer and F. Jellinek, *J. Solid State Chem.*, 1987, **70**, 207–209.
26 A. Klein, S. Tiefenbacher, V. Eyert, C. Pettenkofer and W. Jaegermann, *Phys. Rev. B: Condens. Matter Mater. Phys.*, 2001, **64**, 205416.
27 N. Kumar, S. Najmaei, Q. Cui, F. Ceballos, P. M. Ajayan, J. Lou and H. Zhao, *Phys. Rev. B: Condens. Matter Mater. Phys.*, 2013, **87**, 125427.
28 Y. Li, Y. Rao, K. F. Mak, Y. You, S. Wang, C. R. Dean and T. F. Heinz, *Nano Lett.*, 2013, **13**, 3329–3333.
29 A. R. Khan, B. Liu, T. Lu, L. Zhang, A. Sharma, Y. Zhu, W. Ma and Y. Lu, *ACS Nano*, 2020, **14**, 15806–15815.
30 J. Liang, J. Zhang, Z. Li, H. Hong, J. Wang, Z. Zhang, X. Zhou, R. Qiao, J. Xu, P. Gao, Z. Liu, Z. Liu, Z. Sun, S. Meng, K. Liu and D. Yu, *Nano Lett.*, 2017, **17**, 7539–7543.
31 K. S. Novoselov, F. S. D. Jiang, T. J. Booth, V. V. Khotkevich, S. V. Morozov and A. K. Geim, *Proc. Natl. Acad. Sci. U. S. A.*, 2005, **102**, 10451–10453.
32 J. N. Coleman, M. Lotya, A. O'Neill, S. D. Bergin, P. J. King, U. Khan, K. Young, A. Gaucher, S. De, R. J. Smith, I. V. Shvets, S. K. Arora, G. Stanton, H.-Y. Kim, K. Lee, G. T. Kim, G. S. Duesberg, T. Hallam, J. J. Boland, J. J. Wang, J. F. Donegan, J. C. Grunlan, G. Moriarty, A. Shmeliov, R. J. Nicholls, J. M. Perkins, E. M. Grieveson, K. Theuwissen, D. W. McComb, P. D. Nellist and V. Nicolosi, *Science*, 2011, **331**, 568–571.
33 P. Joensen, R. F. Frindt and S. R. Morrison, *Mater. Res. Bull.*, 1986, **21**, 457–461.
34 J. R. Brent, N. Savjani and P. O'Brien, *Prog. Mater. Sci.*, 2017, **89**, 411–478.
35 B. Mahler, V. Hoepfner, K. Liao and G. A. Ozin, *J. Am. Chem. Soc.*, 2014, **136**, 14121–14127.
36 G. Pippia, D. Van Hamme, B. Martin-Garcia, M. Prato and I. Moreels, *Nanoscale*, 2022, **14**, 15859–15868.
37 N. Kapuria, N. N. Patil, A. Sankaran, F. Laffir, H. Geaney, E. Magner, M. Scanlon, K. M. Ryan and S. Singh, *J. Mater. Chem. A*, 2023, **11**, 11341–11353.
38 A. Niebur, A. Soll, P. Haizmann, O. Strolka, D. Rudolph, K. Tran, F. Renz, A. P. Frauendorf, J. Hubner, H. Peisert, M. Scheele and J. Lauth, *Nanoscale*, 2023, **15**, 5679–5688.
39 M. Frohlich, M. Kogel, J. Hiller, L. Kahlmeyer, A. J. Meixner, M. Scheele, J. C. Meyer and J. Lauth, *Phys. Chem. Chem. Phys.*, 2024, **26**, 13271–13278.
40 Y. Sun, K. Fujisawa, Z. Lin, Y. Lei, J. S. Mondschein, M. Terrones and R. E. Schaak, *J. Am. Chem. Soc.*, 2017, **139**, 11096–11105.
41 G. Pippia, A. Rousaki, M. Barbone, J. Billet, R. Brescia, A. Polovitsyn, B. Martín-García, M. Prato, F. De Boni, M. M. Petrić, A. Ben Mhenni, I. Van Driessche, P. Vandenabeele, K. Müller and I. Moreels, *ACS Appl. Nano Mater.*, 2022, **5**, 10311–10320.
42 A. P. Frauendorf, A. Niebur, L. Harms, S. Shree, B. Urbaszek, M. Oestreich, J. Hübner and J. Lauth, *J. Phys. Chem. C*, 2021, **125**, 18841–18848.
43 A. Dasgupta, X. Yang and J. Gao, *ACS Photonics*, 2020, **7**, 2506–2514.
44 S. Klimmer, O. Ghaebi, Z. Gan, A. George, A. Turchanin, G. Cerullo and G. Soavi, *Nat. Photonics*, 2021, **15**, 837–842.
45 M. Stavrou, N. Chazapis, E. Nikoli, R. Arenal, N. Tagmatarchis and S. Couris, *ACS Appl. Nano Mater.*, 2022, **5**, 16674–16686.
46 V. Pelgrin, H. H. Yoon, E. Cassan and Z. Sun, *Light: Adv. Manuf.*, 2023, **4**(3), 311–333.
47 W. J. Schutte, J. L. De Boer and F. Jellinek, *J. Solid State Chem.*, 1987, **70**, 207–209.
48 A. Berkdemir, H. R. Gutiérrez, A. R. Botello-Méndez, N. Perea-López, A. L. Elías, C.-I. Chia, B. Wang, V. H. Crespi, F. López-Urías, J.-C. Charlier, H. Terrones and M. Terrones, *Sci. Rep.*, 2013, **3**, 1–8.
49 L. Pan, P. Miao, A. Horneber, A. J. Meixner, P. M. Adam and D. Zhang, *Beilstein J. Nanotechnol.*, 2022, **13**, 572–581.
50 X. Wang, K. Broch, R. Scholz, F. Schreiber, A. J. Meixner and D. Zhang, *J. Phys. Chem. Lett.*, 2014, **5**, 1048–1054.
51 A. L. Elías, N. Perea-López, A. Castro-Beltrán, A. Berkdemir, R. Lv, S. Feng, A. D. Long, T. Hayashi, Y. A. Kim, M. Endo, H. R. Gutiérrez, N. R. Pradhan, L. Balicas, T. E. Mallouk, F. López-Urías, H. Terrones and M. Terrones, *ACS Nano*, 2013, **7**, 5235–5242.
52 Y. Liu, X. Hu, T. Wang and D. Liu, *ACS Nano*, 2019, **13**, 14416–14425.
53 X. Xu, L. Li, M. Yang, Q. Guo, Y. Wang, X. Li, X. Zhuang and B. Liang, *Opt. Express*, 2021, **29**, 5856–5866.
54 Q. Cui, Z. Luo, Q. Cui, W. Zhu, H. Shou, C. Wu, Z. Liu, Y. Lin, P. Zhang, S. Wei, H. Yang, S. Chen, A. Pan and L. Song, *Adv. Funct. Mater.*, 2021, 31.
55 T. Kato and T. Kaneko, *ACS Nano*, 2016, **10**, 9687–9694.
56 P. K. Chow, R. B. Jacobs-Gedrim, J. Gao, T.-M. Lu, B. Yu, H. Terrones and N. Koratkar, *ACS Nano*, 2015, **9**, 1520–1527.
57 V. Carozo, Y. Wang, K. Fujisawa, B. R. Carvalho, A. McCreary, S. Feng, Z. Lin, C. Zhou, N. Perea-López, A. L. Elías, B. Kabius, V. H. Crespi and M. Terrones, *Sci. Adv.*, 2017, **3**, 1–9.
58 H. Sun, Q. Yang, J. Wang, M. Ding, M. Cheng, L. Liao, C. Cai, Z. Chen, X. Huang, Z. Wang, Z. Xu, W. Wang, K. Liu, L. Liu, X. Bai, J. Chen, S. Meng and L. Wang, *Nat. Commun.*, 2024, **15**, 9476.
59 Z. Ye, T. Cao, K. O'Brien, H. Zhu, X. Yin, Y. Wang, S. G. Louie and X. Zhang, *Nature*, 2014, **513**, 214–218.
60 C. Poellmann, P. Steinleitner, U. Leierseder, P. Nagler, G. Plechinger, M. Porer, R. Bratschitsch, C. Schüller, T. Korn and R. Huber, *Nat. Mater.*, 2015, **14**, 889–893.
61 S. Zhang, N. Dong, N. McEvoy, M. O'Brien, S. Winters, N. C. Berner, C. Yim, Y. Li, X. Zhang, Z. Chen, L. Zhang, G. S. Duesberg and J. Wang, *ACS Nano*, 2015, **9**, 7142–7150.
62 Y. R. Shen, *Annu. Rev. Phys. Chem.*, 1989, **40**, 327–350.

63 R. I. Woodward, R. T. Murray, C. F. Phelan, R. E. P. D. Oliveira, T. H. Runcorn, E. J. R. Kelleher, S. Li, E. C. D. Oliveira, G. J. M. Fechine, G. Eda and C. J. S. D. Matos, *2D Mater.*, 2016, 4.
64 J.-P. Wang, Y.-Q. Fang, W. He, Q. Liu, J.-R. Fu, X.-Y. Li, Y. Liu, B. Gao, L. Zhen, C.-Y. Xu, F.-Q. Huang, A. J. Meixner, D. Zhang and Y. Li, *Adv. Opt. Mater.*, 2023, **11**, 2300031.
65 C. Janisch, Y. Wang, D. Ma, N. Mehta, A. L. Elias, N. Perea-Lopez, M. Terrones, V. Crespi and Z. Liu, *Sci. Rep.*, 2014, **4**, 5530.
66 L. Pan, P. Miao, A. Horneber, A. J. Meixner, P.-M. Adam and D. Zhang, *ACS Appl. Nano Mater.*, 2023, **6**, 6467–6473.
67 J. Hernandez-Rueda, M. L. Noordam, I. Komen and L. Kuipers, *ACS Photonics*, 2021, **8**, 550–556.